Corrosion behavior of 2024 Al−Cu−Mg alloy of various tempers

K. S. GHOSH, Md. HILAL, Sagnik BOSE

Department of Metallurgical and Materials Engineering, National Institute of Technology, Durgapur – 713 209, India

Abstract: Corrosion behavior of 2024 Al−Cu−Mg alloy of different tempers was assessed by potentiodynamic polarization studies in 3.5% NaCl solution, 3.5% NaCl+1.0% H_2O_2 solution and 3.5% NaCl solution at pH 12. Polarization curves showed shifting of corrosion potential (φ_{corr}) towards more negative potential with increasing ageing time and shifting of φ_{corr} in the positive direction with the addition of H_2O_2 in NaCl solution. Polarization curves in 3.5% NaCl solution at pH 12 exhibited distinct passivity phenomenon. Optical micrographs of the corroded surfaces showed general corrosion, extensive pitting and intergranular corrosion as well. Cyclic potentiodynamic polarization curves exhibited wide hysteresis loop and the mode of corrosion attack confirmed that the alloy states are susceptible to pit growth damage. Attempts were made to explain the observed corrosion behavior of the alloy of various tempers in different electrolytes with the help of microstructural features.
Key words: 2024 Al−Cu−Mg alloy; ageing behavior; electrochemical polarization; passivity; pitting potential

1 Introduction

Precipitation hardening aluminium alloys of 2xxx series with high specific strength, good fracture toughness, excellent fatigue properties and damage tolerance have been found important applications in the aerospace industry. In commercial 2xxx series alloys, Cu and Mg are the main alloying elements with small amount of Si and other minor elements such as Mn, Zn, Ti and Fe [1−3]. Depending on the concentrations of Cu, Mg and Si, these 2xxx series aluminium alloys may span as many as five phase fields, including up to five equilibrium phases, such as those designated as θ, S, Si, Mg_2Si and Q [2,4]. Among the commercial 2xxx series alloys, the 2024 alloy which is in the $\alpha+S+\theta$ phase field, is particularly important, due to its widespread applications as an aeroplane wing and fuselage outer skin [1,4].

Aluminium alloys derive their strength from deliberately developed heterogeneous microstructures that consist of a combination of hardening precipitates, dispersoids, and constituent particles formed through appropriate solution heat treatment (SHT) and ageing schedules. The results of earlier studies essentially showed that the microstructure of the 2024 alloy with a mass ratio of Cu to Mg 2.93 has been dominated by

microscale S (Al_2CuMg) phase, nanoscale dispersoid ($Al_{20}Mn_3Cu_2$) particles along with a significant amount of other microscale intermetallic particles containing Al, Cu, Fe, and Mn, such as, θ(Al_2Cu), Al_3Fe, Al_3Mn, Al_7Cu_2Fe, and $(Al,Cu)_6Mn$, distributed throughout the matrix [3,5,6]. Often some of these particles are observed to cluster very closely together or even fuse, demonstrating the highly complex nature of the 2024 alloy microstructure.

In general, the approaches that improve mechanical properties through microstructural modifications result in detrimental changes to corrosion properties, namely, an inverse relationship exists between the strength and the corrosion resistance in precipitation hardenable 2xxx, 6xxx and 7xxx series aluminium alloys. It has been, generally, observed that the stronger these types of alloys are, the poorer the corrosion resistance is [7], especially to stress corrosion cracking (SCC) resistance.

The matrix strengthening precipitates and many intermetallics present in the 2024 alloy microstructure are heterogeneous from an electrochemical perspective. This renders the alloy and similar class of alloys are susceptible to localized corrosion resulting from local galvanic cells and variation in passive film stability between solute-rich second phase particles and the matrix [8−11]. Specifically, Cu-rich precipitates and intermetallics are known to act as, or eventually become

local cathodes, which facilitate oxygen reduction reactions and ultimately drive anodic dissolution of the surrounding matrix material [12].

Thus, in view of the maintenance of aircrafts and their long-term use, it is important to characterize the corrosion behavior (micro- and nano-scale level) and mechanism of corrosion attack influenced by the alloy microstructure. Further, for a longer service life and resistance to sudden catastrophic failure, it is essentially required that the aircraft structures would resist to undergo localized corrosion and environmental assisted cracking (EAC), e.g. stress corrosion cracking (SCC), hydrogen embrittlement (HE) and corrosion fatigue (CF) [13,14] .

Localized corrosion behavior of 2024 alloy with varying Cu and Mg content has been studied in details [6,15−23]. The localized corrosion susceptibility is affected in the presence of S (Al_2CuMg) and inhomogeneous second phase particles. The localized corrosion studied by micropolarization showed that the Al 2024 alloy with lower Mg content (Cu to Mg mass ratio of 3.7) is significantly different from the 2024 alloy with a more common composition (Cu to Mg mass ratio of 2.9). The localized corrosion (microscale and nanoscale level) initiation behavior of the Al 2024 alloy with a more common composition showed a clear separation of the distribution of the measured pitting potentials for S phase and intermetallic AlCuFeMn particles with variable stoichiometry, and matrix areas. Characterization of the microstructure and its relation to the localized corrosion initiation properties of the 2024-T351 alloy have been done to provide both qualitative and quantitative input data (microstructural geometry and microscale electrochemical measurement data) for development of microscale and macroscale numerical models and simulations of corrosion.

Further, a lot of research work and literatures [24−28] are available on corrosion protection of Al alloys by chromate based conversion coating, application of primer and other means. But, the chromate compounds are highly toxic and carcinogenic, so there is an urgent need of development of alternative corrosion inhibitors for protecting aluminium alloy. Among these new inhibitors, rare earth salts were tested to be effective and environmental benign inhibitors. The inhibiting effect of cerium cation on corrosion of aluminium alloy was reported to be due to the shifting of cathodic oxygen reduction reaction by the formation of oxides and hydroxides of Ce(III), La(III) and Al_2O_3 [28−34].

There are many investigations [15−23] on the influence of matrix strengthening phases and intermetallic particles on the localized (nano- and micr-oscale level) corrosion of 2024 alloy with different Cu to Mg ratios, and the critical particle size below which localized corrosion is not affected, but there is a scanty literature on systematic study of corrosion behavior of the 2024 alloy with ageing time and different tempers, i.e. as-quenched, under-, peak- and over-aged tempers. Since the 2024-T3 alloy is being used in structural components of aircraft, it is appropriate to assess the corrosion behavior with ageing time of the alloy in different tempers. Hence, in the present investigation, attempts are made to correlate the ageing and corrosion behavior of a 2024 alloy of various tempers, such as as-quenched, under-, peak- and over-aged in the electrolytes of 3.5% NaCl solution, 3.5% NaCl+1.0% H_2O_2 solution near neutral pH and 3.5% NaCl solution at pH 12.

2 Experimental

2.1 Materials

2024 Al−Cu−Mg alloy in square bar shape with dimensions of 15 mm×6.35 mm×6.35 mm was procured from Alfa Aesar (A Johnson Matthey Company) Ward Hill, MA 01835, USA. The chemical compositions of the 2024 alloy are given in Table 1. The grains of the alloy are polygonal with an average size of 25−30 μm. Specimens with dimensions of 6.35 mm×6.35 mm× 3 mm (approximately) were cut from the square alloy rod for heat treatment and subsequent other studies.

Table 1 Chemical compositions of 2024 alloy (mass fraction, %)

Cu	Mg	Mn	Fe	Si	Cr	Al
4.40	1.50	0.60	< 0.50	< 0.50	< 0.10	Bal.

2.2 Ageing treatment to produce various tempers

A large number of specimens cut from the as-received 2024 alloy square bar were subjected to solution heat treatment (SHT) at temperature of 490 °C for 30 min, water quenched at room temperature followed by artificial ageing at temperature of 190 °C for varying time up to 154 h corresponding to over-aged state, and a sample was also naturally aged for prolonged time. The details of various ageing schedules and designated alloy tempers produced for the present investigation are stated in Table 2.

2.3 Hardness testing

Vicker's hardness tester, Model BV250(S), was used for measuring the hardness of the alloys of various tempers in order to assess the natural and artificial ageing

Table 2 Heat treatment, ageing schedules and designated tempers of 2024 alloy

Temper designation	Ageing schedule
2024-AQ	2024 alloy is solutionised at 490 °C for 30 min followed by water quenching
2024-NA-720h	2024-AQ state alloy is naturally aged at room temperature for 30 d, i.e. 720 h
2024-190-*x*h	2024-AQ state alloy is artificially aged at temperature of 190 °C for *x* h. For example: 2024-190-1 h stands for 2024-AQ state alloy is artificially aged at temperature 190 °C for 1 h

behavior of the alloy. The load applied for measuring hardness was 98 N and the reported value of hardness was an average of at least three readings.

2.4 X-ray diffraction

X-ray diffraction (XRD) was carried out to acquaint with the various phases present in the alloy of different tempers. XRD study was carried out using a PANlytical XPert Pro basic X-ray diffractometer unit with Cu K_α radiation.

2.5 SEM, EDAX analysis and elemental mapping

X-ray elemental mapping of the 2024 alloy was studied by using a scanning electron microscope (SEM), Model Hitachi S−3000 N, with an EDAX attachment.

2.6 Electrochemical polarisation

Potentiodynamic polarizations were carried out on the samples of alloy with various tempers, e.g. 2024-AQ, 2024-190-1 h, and 2024-190-154 h, as stated in Table 2, using a computer controlled VoltaLab potentiostat/galvanostat (Model PGP201) with an inbuilt Voltamaster4 software. Experiments were carried out by constructing a local electrochemical cell using the standard three electrodes configuration: saturated calomel electrode (SCE) as a reference, a platinum plate as a counter electrode and the sample as the working electrode. Polarization scan was carried out towards more noble value at a scan rate of 0.50 mV/s, after allowing a steady state potential to develop. The electrolytes used for the polarization studies were 3.5% NaCl solution and 3.5% NaCl+1.0% (volume fraction) H_2O_2 solution at near neutral pH and 3.5% NaCl solution at pH 12 as well. The pH 12 was obtained by adding a small amount of NaOH to 3.5% NaCl solution.

In order to assess the pit protection potential (φ_{prot}), cyclic potentiodynamic polarization studies were carried out on a few alloy tempers in 3.5% NaCl solution at pH 12. Samples were polarized below the φ_{prot} potential and the microscopic study revealed no pitting. In order to

confirm whether pitting damage or pit repassivation has occurred below the φ_{prot}, further potentiodynamic polarization study on a few alloy tempers was also run below the pit protection potential, and the corroded surfaces were observed.

2.7 Observation of corroded surfaces

In order to assess the type and morphology of corrosion attack upon electrochemical polarization studies of these alloy tempers in different environments, an optical microscope (model LEICA DM 2500M) with an inbuilt QWin3 software was used to observe the corroded surfaces. The corroded surface were observed in as-such situation or often gently disk polished to remove the covered oxide/corroded layer.

3 Results and discussion

3.1 Ageing behavior of 2024 alloy

Figure 1 shows the age hardening behavior of the 2024 alloy solution heat treated, water quenched followed by artificial ageing at temperature of 190 °C, and natural ageing as well. The variation of hardness with ageing time displayed the characteristic age hardening behavior of precipitation hardenable aluminium alloys, namely with increasing ageing time, there is a progressive increase of hardness, reaching a maximum value (peak aged temper) and subsequent decrease of hardness with further ageing leading to over-aged state.
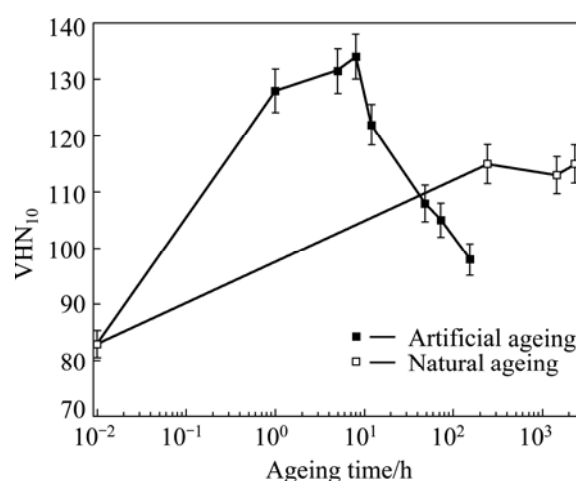

Fig. 1 Variation of hardness with ageing time of 2024 alloy solution heat treated, water quenched followed by artificial and natural ageing

In the Al−Cu system, the most explained precipitation sequence is GP zones, coherent θ'', semi-coherent θ', and finally equilibrium θ(Al_2Cu) phase. Small addition of magnesium affects the formation of coherent phase and facilitates the precipitation of

semi-coherent θ' phase, and generally increases the hardening effect [1,35,36]. Further, the increase of magnesium concentration results in the formation of S (Al$_2$CuMg) phase; and the precipitation sequence is similar to that of the Al$_2$Cu phase: Guinier-Preston-Bagaryatsky zones, coherent S'', semi-coherent S', and equilibrium S. The structure of all S-phases are very close, and literatures suggested them as a structure differently distorted due to coherent or semi-coherent junctions with the matrix [1,35−41].

It was proposed that in Al−Cu−Mg alloys, two stages of hardening occur. An early rapid rise in hardness is due to the formation of fine scale (average 24 atoms) solute clusters of Mg and Cu; Mg−Mg aggregates were the first to appear, followed by Cu−Cu aggregates and Cu−Mg clusters due to the higher binding energy between Mg atoms and vacancies. The second stage of hardening (peak aged state) is dominated by S phase in the form of laths with the $\{120\}_{Al}$ habit plane elongated along $\langle100\rangle_{Al}$ direction [35,42−43]. Recent work has shown that a semi-coherent phase designated by S'' or GPB2 with orthogonal structure occurs well before peak hardness is reached and remains in the matrix in peak aged state [35,43]. In over aged state, the microstructure comprises coarse S phase with a range of morphologies, including rods with an aspect ratio (the ratio of width to thickness) 3:1 and irregular cross-sections (i.e. agglomeration of rods) [40,44,45], and no presence of GPB zones or solute clusters. All these justify the drop of hardness in the over aged state.

3.2 XRD pattern

Figure 2 shows the XRD pattern of 2024 alloy in three artificially aged states, using Cu K$_\alpha$ radiation. The patterns of all the tempers indicate the peaks of all the probable phases such as α(Al), intermetallic S' (Al$_2$CuMg), Al$_7$Cu$_2$Fe and θ' (Al$_2$Cu) phases that would
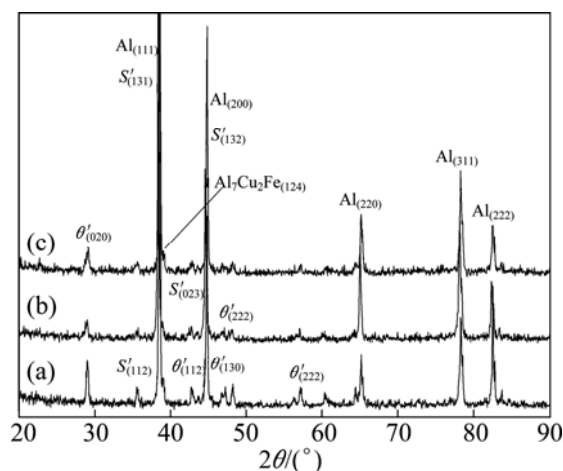

Fig. 2 XRD patterns of 2024 alloy of various tempers: (a) 2024-190-1h; (b) 2024-190-5h; (c) 2024-190-150h

be present in the alloy system. However, there may be presence of other intermetallic phases, being reflected with smaller peaks, but difficult to confirm from the XRD patterns.

3.3 SEM and elemental mapping

Figure 3 exhibits a SEM image and X-ray elemental mapping of alloy 2024-190-8h. Figure 3(a) shows grains of α(Al) matrix and the presence of a large number of intermetallics. The X-ray elemental mapping shows that aluminium is uniformly and densely distributed over the entire matrix. Further, the uniform distribution of Cu and Mg indicates the presence of equilibrium S (Al$_2$CuMg) phase within the matrix, as the observed microstructure in the order of micron. However, Figures 3(d) and (e) exhibit the distribution of Fe and Mn mostly in the intermetallics regions of the microstructure. Also there is a lean distribution of Fe and Mn preferably and probably along the sub- and grain boundaries.

3.4 Potentiodynamic polarization

Figure 4 shows the potentiodynamic polarization curves of 2024 alloy of various tempers in 3.5% NaCl, 3.5% NaCl+1.0% H$_2$O$_2$ at near neutral pH and in 3.5% NaCl at pH 12 solutions, respectively.

The shape of the polarization curves in Figs. 4(a) and (b) is similar for all the tempers. In all the cases, the cathodic and anodic branches of the curves show typical potential−current density characteristics of aluminium alloy system in 3.5% NaCl solution at near neutral pH. However, the polarization curves in Fig. 4(c) in 3.5% NaCl solution at pH 12 show clearly the acitve−passive−transpassive phenomenon.

The cathodic branches of the polarization curves showing the typical Tafel behavior enable to evaluate cathodic slope or Tafel constant (β_c) as well as corrosion current density (J_{corr}) by Tafel extrapolation method. The anodic branches of the polarization curves in 3.5% NaCl and 3.5% NaCl+1.0% H$_2$O$_2$ solutions exhibit typical active metal dissolution behavior with an initial sharp increase of corrosion current density under applied anodic overvoltage, and then further increase of current density under higher anodic overvoltage.

In 3.5% NaCl solution at pH 12, the anodic branches of the polarization curves for all the alloy tempers exhibit active, spontaneous passive, passive and transpassive regions. In the active region, metal dissolution occurs increasingly with the increase of applied anodic overvoltage, reaching maximum current density, which is called critical current density (J_{crit}). But, beyond the critical current density, the decrease of current density with increasing overvoltage is due to the beginning of formation of passive oxide layer (state of spontaneous passivation), attaining a stable passive state
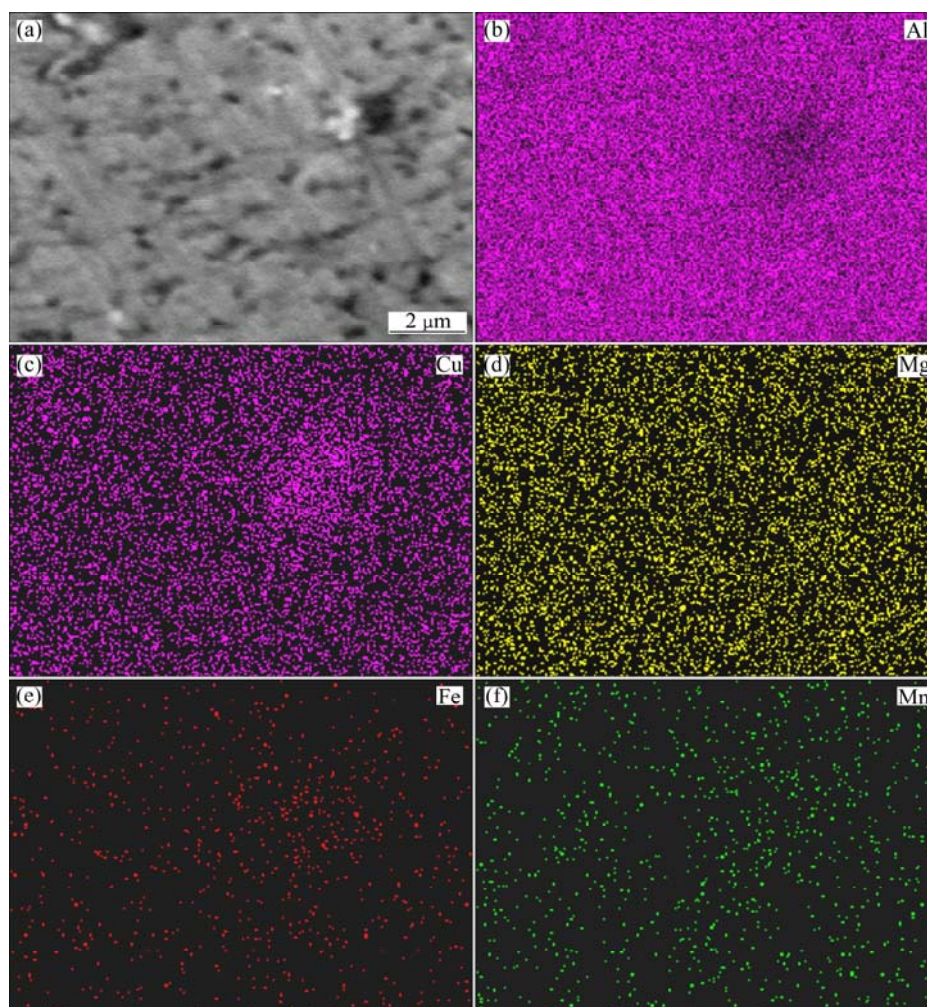
Fig. 3 SEM image (a) and X-ray mappings (b−f) of 2024-190-8h alloy

with a constant low current density (passive current density, J_p) over a passive potential range (φ_{pp}). With the further increase of applied potential, the current density increases sharply, and this potential is considered oxide break-down (φ_{bd}) or pitting potential (φ_p), leading to localized corrosion, i.e. pits formation with rapid metal dissolution.

Tables 3 and 4 give the electrochemical data, such as corrosion potential (φ_{corr}), corrosion current density (J_{corr}), critical current density (J_{crit}), passive potential range (φ_{pp}), passive current density (J_p) etc, obtained from these polarization curves of the 2024 alloy of various tempers.

The electrochemical behavior of the 2024 alloy with heterogeneous microstructure, in general, depends on the degree of segregation, clustering, the morphology and distribution of precipitates and intermetallics, the relative areas of exposed phases, the electrode kinetics of each phase, and the development of electrochemical local cells among them, etc. Therefore, the complexity (in terms of number of phases and intermetallics present) in the alloy microstructure and the problem of judicious selection of cathodic Tafel's region impose limitations and errors in finding out the corrosion current density, J_{corr} [2,8,21,35,36,39−41,44]. However, these reported electrochemical data give an idea of electrochemical performance of the alloy tempers, although the reported J_{corr} values (Tables 3 and 4) determined by Tafel extrapolation technique may vary by ±15%.

A close look of the corrosion current density (J_{corr}) of various alloy tempers in a given environment seems to be more or less same within an order of variation and or within the error limits of Tafel extrapolation method. But, certainly there must be a definite effect of variation of corrosion behavior of various alloy tempers having different ageing time. This is because in different alloy tempers (from as-quenched (AQ) state to under- to peak- to over-aged tempers), there are variations of solute contents in α(Al) matrix, differences of size, distribution of GPB zones and S'/S (Al$_2$CuMg) phase and their
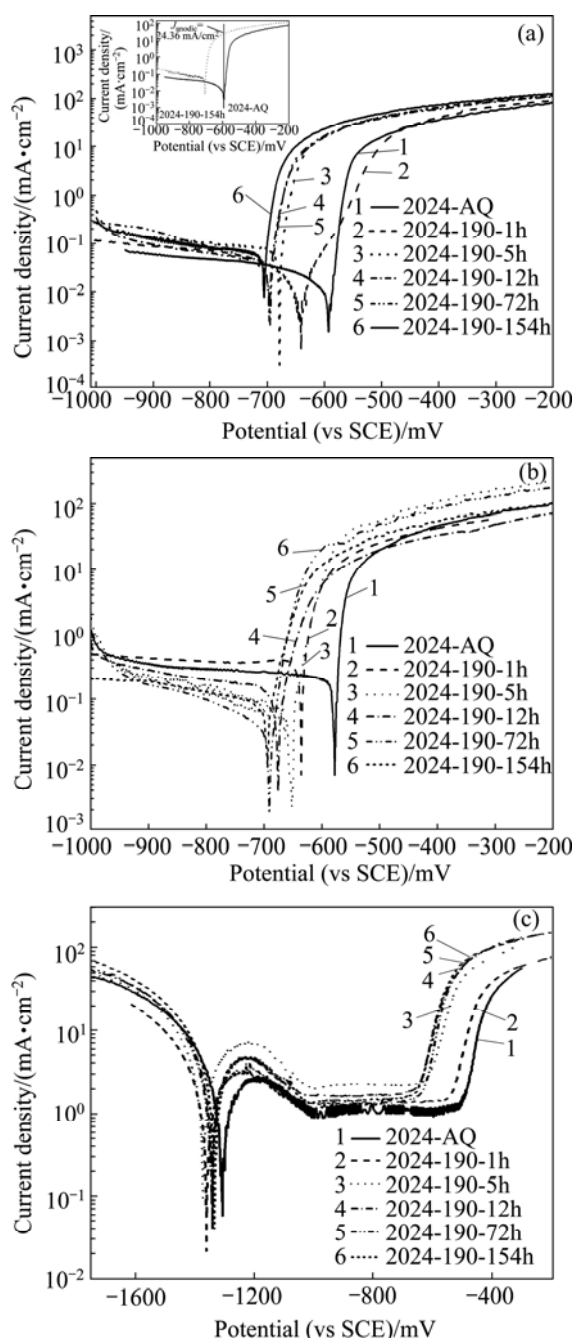
Fig. 4 Potentiodynamic polarization curves of 2024 alloy of different tempers: (a) In 3.5% NaCl solution; (b) In 3.5% NaCl+10% H₂O solution; (c) In 3.5% NaCl solution at pH 12

variant as well. In the as-quenched state, the α(Al) solid solution is supersaturated with solutes of Cu, Mg and Mn, but, as ageing progresses, the α solid solution gets solute depleted and there is precipitation of GPB zones and S'/S phase (as discussed in section 3.1) in the presence of other intermetallics as well. In the context, it is to state that copper is electrochemically cathodic and the S'/S phase is more anodic (more negative potential) with respect to the matrix α solid solution [46,47].

The expected variation of corrosion behavior of the alloy with different ageing time has been explained by

Table 3 Electrochemical data of 2024 alloy of various tempers in 3.5% NaCl solution and 3.5% NaCl+1.0% H₂O₂ solution

Alloy temper	Solution	φ_{corr} (vs SCE)/ mV	J_{corr}/ (mA·cm^{-2})	J_{anodic} (at φ_{corr} of AQ state)/ (mA·cm^{-2})
2024-AQ		−593	0.022	−
190-1h		−640	0.039	0.105
190-5h	3.5% NaCl	−678	0.069	17.76
190-12h		−696	0.041	16.70
190-72h		−695	0.05	17.30
190-154h		−706	0.055	24.36
2024-AQ		−579	0.21	−
190-1h		−637	0.305	10.66
190-5h	3.5% NaCl + 1.0% H₂O₂	−651	0.078	22.40
190-12h		−677	0.124	9.40
190-72h		−691	0.066	24.72
190-154h		−696	0.086	16.80

Table 4 Electrochemical data of 2024 alloy in 3.5% NaCl solution at pH 12

Alloy temper	J_{crit}/ (mA·cm^{-2})	φ_{corr}(vs SCE)/ mV	J_p/ (mA·cm^{-2})	φ_p(vs SCE)/ mV	φ_{prot}(vs SCE)/ mV
2024-AQ	2.61	−1304	1.12	−1005 − −511	
190-1h	3.36	−1358	1.35	−1040 − −561	
190-5h	6.82	−1320	2.27	−1006 − −618	
190-12h	4.68	−1338	1.65	−1039 − −663	
190-72h	3.98	−1342	1.36	−1012 − −661	
190-154h	4.62	−1337	1.46	−1020 − −671	
Cyclic polarisation					
190-1h	4.32	−1350	1.85	−1039 − −553	−852
190-5h	3.95	−1318	1.48	−1008 − −593	−842
Polarisation below φ_{prot}					
190-5h	3.61	−1331	1.53		
190-12h	3.88	−1324	1.02		
190-72h	4.51	−1315	1.79		

comparing the corrosion current density of the polarization curves of various tempers with respect to J_{corr} at φ_{corr} of the as-quenched state. The polarization curves show that the current densities of the alloys with higher ageing time have been found to be anodic (denoted in this paper as J_{anodic}) and much higher with respect to J_{corr} of the as-quenched (AQ) state. The way of

finding out J_{anodic} of the 2024-190-152h alloy with respect to the J_{corr} (at φ_{corr}) of the 2024-AQ is shown in inset of Fig. 4(a). Similarly, J_{anodic} values have been calculated for other tempers and mentioned in Tables 3 and 4. Thus, it is appropriate to infer that the current density and thereby the corrosion rate increase with ageing time. Polarization curves of intermetallics and phases present in aluminium alloys have also been shown and compared in similar way [17].

3.4.1 Electrolyte and its condition

In 3.5% NaCl solution at near neutral pH, the anodic current density is low (uniform corrosion is repressed by natural oxide layer) and the cathodic current density arising from the number of precipitates and intermetallics acting as local cathodes and the volume of oxidants, e.g. dissolved oxygen in the electrolyte, is dominating; and the summary current density (anodic plus cathodic current density) is negative and low. The corrosion potential (φ_{corr}) is in the pitting potential (φ_{br}) range (Tables 3 and 4), and this implies that the alloy will corrode under free corrosion potential.

Comparison (for a given alloy temper) of the potentiodynamic polarization curves in 3.5% NaCl and in 3.5% NaCl + 1.0% H_2O_2 solutions (Figs. 4(a) and (b) and Tables 3 and 4) shows that φ_{corr} values have shifted towards positive direction with the addition of small amount of H_2O_2 in 3.5% NaCl solution. This is clearly seen from Figs. 5(a)−(f), the polarization curves for a
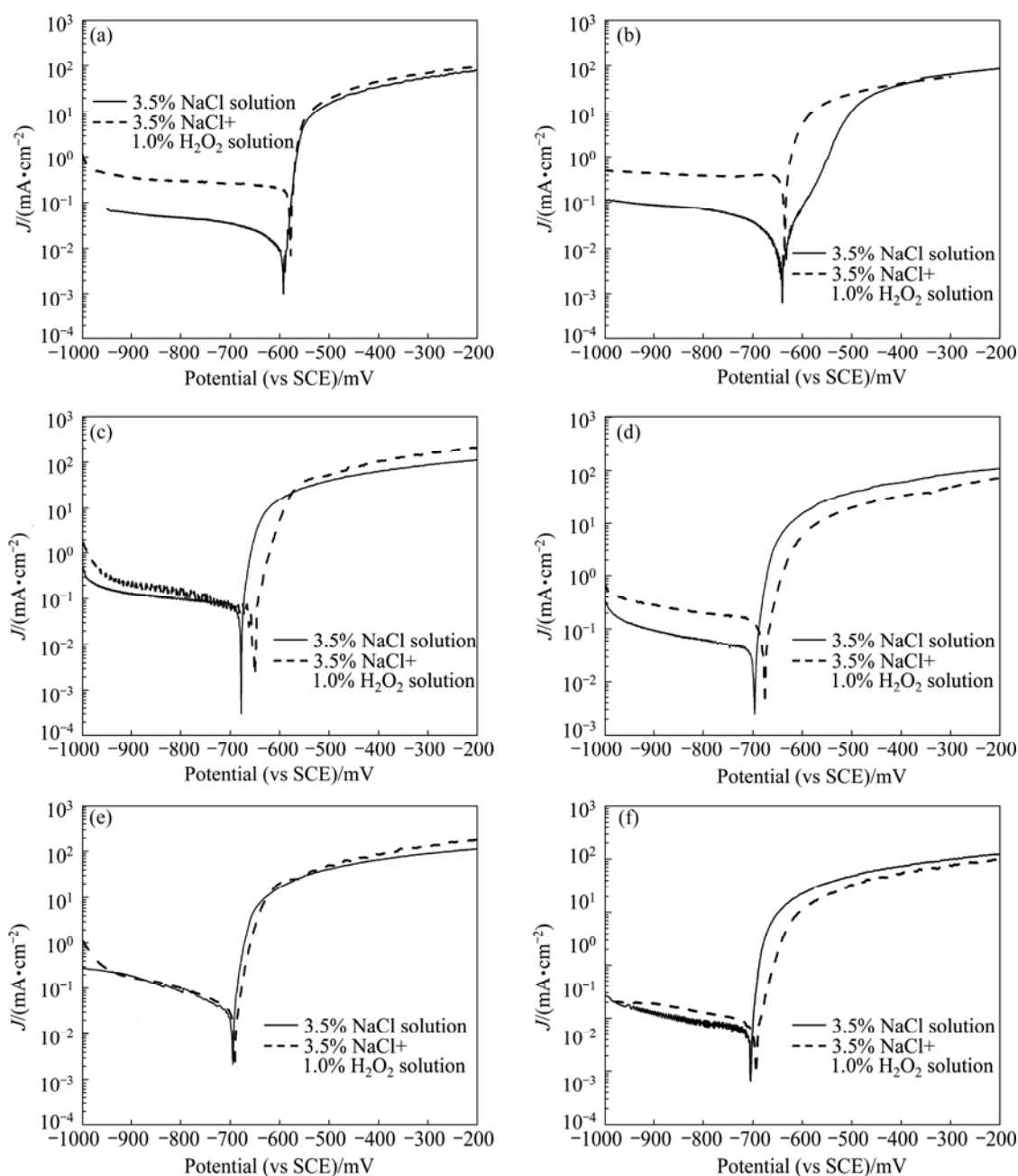

Fig. 5 Potentiodynamic polarisation curves of 2024 alloy in different temper states in 3.5% NaCl and 3.5% NaCl+1.0% H_2O_2 solutions: (a) 2024-AQ; (b) 2024-190-1h; (c) 2024-190-5h; (d) 2024-190-12h; (e) 2024-190-72h; (f) 2024-190-154h

given temper in 3.5% NaCl and 3.5% NaCl+1.0% H_2O_2 solutions. The aggressive depassivating nature of the 3.5% NaCl solution makes the alloy bare, but the addition of 1.0% H_2O_2 (volume fraction) shifts the corrosion potential to slightly more positive values due to more oxygen availability in solution, causing to increase the thickness of the oxide layer, to maintain the passive oxide layer and to heal the destroyed oxide layer as well. The difference between φ_p (pitting potential) and φ_{corr} value of the environment containing H_2O_2 is less compared to that in only 3.5% NaCl solution (Table 5). Thus, the environment containing small amounts of H_2O_2 will be more aggressive for localized attack, intergranular corrosion (observed in the present study and discussed in section 3.4.3) and susceptible to environmental assisted cracking (EAC) [13,14], compared to that in only 3.5% NaCl solution. Further, in 3.5% NaCl + 1.0% H_2O_2 solution, the cathodic corrosion reaction (and so the cathodic current density) is increased (as more oxygen available to be reduced) and has to be compensated with a higher anodic current density (dissolution of aluminium). This also accounts for an increase of corrosion current density (J_{corr}) in 3.5% NaCl solution having a small amount of H_2O_2. In the anodic region of the polarization curves, although the current density is initially higher, the curves tend to converge at higher applied anodic potential corresponding to high value of current density.

The dissolution of aluminium, the effect of chloride accelerating attack, and the state for precipitation of $Al(OH)_3$ etc have been stated in Refs. [48,49].

In the alkaline solution, the anodic current density (dissolution of aluminium) is dominating and the summary current density is positive, resulting in shifting the corrosion potential (φ_{corr}) to negative values (negative threshold of passive area) than the pitting potential. In Al alloys, pH of solution has limited effect on the pitting potential but does affect the open circuit potential [50,51]. Potentiodynamic polarizations curves (Figs. 4(c)) of the various alloy tempers in 3.5% NaCl solution at pH 12 showing the distinct passive region which is associated with the formation of thin passive film on the surface.

The main factors controlling the passivation process are the potential of the alloys, the concentration of metallic ion and the interfacial pH. Figure 4(c) also displays that at very negative potential, the current density is higher (approximately 100−400 times) compared to that at near neutral pH solution (Figs. 4(a) and (b)). This is attributed to the fact that at very negative potential, there is higher uniform corrosion; as water splits into H^+ and OH^-, the OH^- causes an pH increase on the aluminium surface. Under this situation, aluminium is dissolved due to missing stability of the natural oxide layer resulting in an increase of current density in negative direction. In the positive potential direction beyond the passive range, the passive area is limited by the pitting potential (φ_p or φ_{br}), localized pitting corrosion occurs. The more the applied potential exceeds in the transpassive region, and the higher the current density is.

The pitting potential (φ_p) may be confounded by the density of precipitate phases (S and θ) serving as pit initiation sites, presence of Cu depletion zones, the oxide film thickness and defects in the oxides at risk surface areas, etc. Since repassivation potential (φ_{rp}) is associated with the repassivation of large pits which seem to be over a hundred times larger than any likely Cu-depleted zones. It is believed that they reflect the corrosion properties of the matrix.

3.4.2 Alloy tempers

Figures 4(a) and (b) and Tables 3 and 4 show that the corrosion potential values, φ_{corr}, shift towards more negative direction with the increase of ageing time. The φ_{corr} value of the over-aged temper is found to be the most negative and for the as-quenched state it is the least negative. In 2024 alloy, the observed shifting of φ_{corr} towards more negative direction with increasing ageing time is due to the reduction of copper content in solid solution and the formation of S (Al_2CuMg) precipitate as well [47]. It is well known that the preferred sites for pitting corrosion initiation in 2024 Al alloy are the S phase precipitates. But, the θ and second intermetallic phases (e.g. AlCuFeMnSi) have better resistance to localized corrosion [5,10,15,16,21].

Therefore, to elucidate the effect of alloy tempers

Table 5 Values of $\Delta(\varphi_p-\varphi_{corr})$ and passive potential range of various 2024 alloy tempers in different media

Alloy temper	φ_p(vs SCE)/ mV	3.5% NaCl solution at pH 12		3.5% NaCl solution		3.5% NaCl+1.0% H_2O_2 solution	
		φ_{pp}(vs SCE)/ mV	$(\varphi_p-\varphi_{corr})$ (vs SCE)/mV	φ_{corr}(vs SCE)/ mV	$(\varphi_p-\varphi_{corr})$ (vs SCE)/mV	φ_{corr}(vs SCE)/ mV	$(\varphi_p-\varphi_{corr})$ (vs SCE)/mV
2024-AQ	−511	494	793	−593	82	−579	68
190-1h	−561	479	797	−640	79	−637	76
190-5h	−618	388	702	−678	60	−651	33
190-12h	−663	376	675	−696	33	−677	14
190-72h	−661	351	681	−695	34	−691	30
190-154h	−671	349	666	−706	35	−696	25

and ageing time on corrosion damage, other than J_{corr} determined by Tafel extrapolation and J_{anodic} (as explained in previous section 3.4.1), the calculation of difference between φ_p and φ_{corr} (or OCP), i.e. $\varphi_p-\varphi_{corr}$, of various alloys may be significant. Table 5 gives the ($\varphi_p-\varphi_{corr}$) values and absolute value of passive potential range ($|\varphi_{pp}|$) at solution pH 12 for all the alloy tempers in all the environments.

The difference between φ_p and φ_{corr} in a given environment is a measure of safety and is also used as a measure of the susceptibility to localized corrosion. The more noble the φ_p with respect to φ_{corr} is the less the alloy is susceptible to initiation of localized corrosion. A useful concept for safety against the transition to local corrosion is that $\varphi_{corr}\ll\varphi_{bd}$ and φ_{prot}, where φ_{bd} is often associated with the stabilization of local corrosion and φ_{prot} is associated with repassivation. When such situation exists, the chance of local high-rate corrosion process is often low [46,52]. The observed higher values of ($\varphi_p-\varphi_{corr}$) and absolute φ_{pp} of the as-quenched and the least values for the highest ageing time alloy state (Table 5) suggest that corrosion increases with the increase of ageing time, as also discussed in Refs. [21,46,52].

Pitting potential, φ_p, is not always an accurate measure of the resistance to pitting of an alloy, for a variety of reasons. The value of φ_p was taken as the characteristic potential where there was a permanent, significant increase of (i.e. 1−2 orders of magnitude) the current density and an increase of dJ/dE. Pit protection (φ_{prot}) or repassivation potential (φ_{rp}) is often defined as the best noble potential at which pits, once formed, will propagate. But, below this potential, pits repassivate, i.e. φ_{rp} or φ_{prot} was measured as the characteristic potential at which there was a significant decrease in pit growth current.

Therefore, in order to assess the protection or repassivation potential of the 2024 alloy tempers, cyclic potentiodynamic polarization curves of two alloy tempers carried out in 3.5% NaCl solution at pH 12 are shown in Fig. 6. The obvious cathodic branch and anodic branch on forward scan exhibit similar trends shown in Figs. 4(c), but on the reverse scan in the anodic branch, there is a nose (with a window of rapid decrease of current density) within the vicinity of passive region of the forward scan. The nose is not intersecting the passive line; however, intersecting exists only in the active region of anodic branch of forward scan. Thus, there is a wide hysteresis/loop between forward and backward scan. Generally, alloys susceptible to pitting corrosion exhibit a large hysteresis. Thus, the area under the curve (hysteresis loop) for the forward and reverse scan for a susceptible alloy is a qualitative measure of corrosion damage due to pit growth. The difference of potential between pitting potential and protection potential is also

used to assess pitting damage. A glance of Fig. 4 and Tables 3 and 4 indicates that the φ_{corr} values of all the alloy tempers in 3.5% NaCl and in 3.5% NaCl+ 1.0% H_2O_2 solutions are higher than the φ_p of the alloy (i.e. $\varphi_{corr}>\varphi_{br}$). That is why extensive pitting has occurred in all the alloy tempers, as shown in Fig. 7.
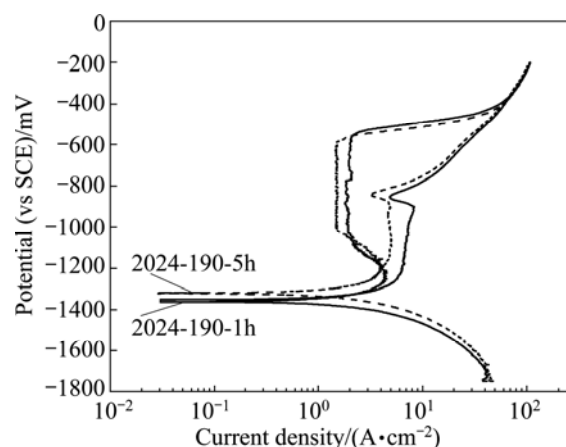

Fig. 6 Cyclic potentiodynamic polarization curves of 2024 alloy of different tempers in 3.5% NaCl solution at pH 12

3.4.3 Corroded surfaces

Figure 7 shows the optical micrographs of the corroded surfaces of the 2024 alloy of various tempers potentiodynamically polarized in the test environments. The corroded surface was observed as such or before observation the surface was gently disk polished to remove the covered oxide/corroded layer. Extensive pitting in all the alloy tempers is seen; pits are seen to be an individual and clusters as well. Further pits mouths are covered with corrosion products. When the alloy is tested in 3.5% NaCl+1.0%H_2O_2 solution, intense intergranular attack takes place. The propensity of more corrosion damage, pitting as well as intergranular attack in 3.5%NaCl+1.0%H_2O_2 solution, is due to additional cathodic reaction facilitated by H_2O_2. Similar corrosion attack, i.e. for individual and cluster of pits, covering of pits mouth with corrosion products, is also seen (Fig. 7(d)) for the alloy polarized in 3.5% NaCl solution at pH 12. A dark field image (Fig. 7(e)) of the corroded surface clearly exhibits a thick covering of corrosion products and pits in its underneath as well.

The cyclic potentiodynamic polarization (Fig. 6) curves, showing large hysteresis loop with not well defined intersecting point of reverse scan (but with a small window of decrease of current density) with the passive line of forward scan, rather intersecting at active region, indicate no well defined repassivation (φ_{rp}) or pit protection (φ_{prot}) potential in 3.5% NaCl at pH 12 solution. To confirm this observation, i.e. whether the alloy tempers are resistant to stable pit growth or pit may be in embryonic state below φ_{prot} potential,
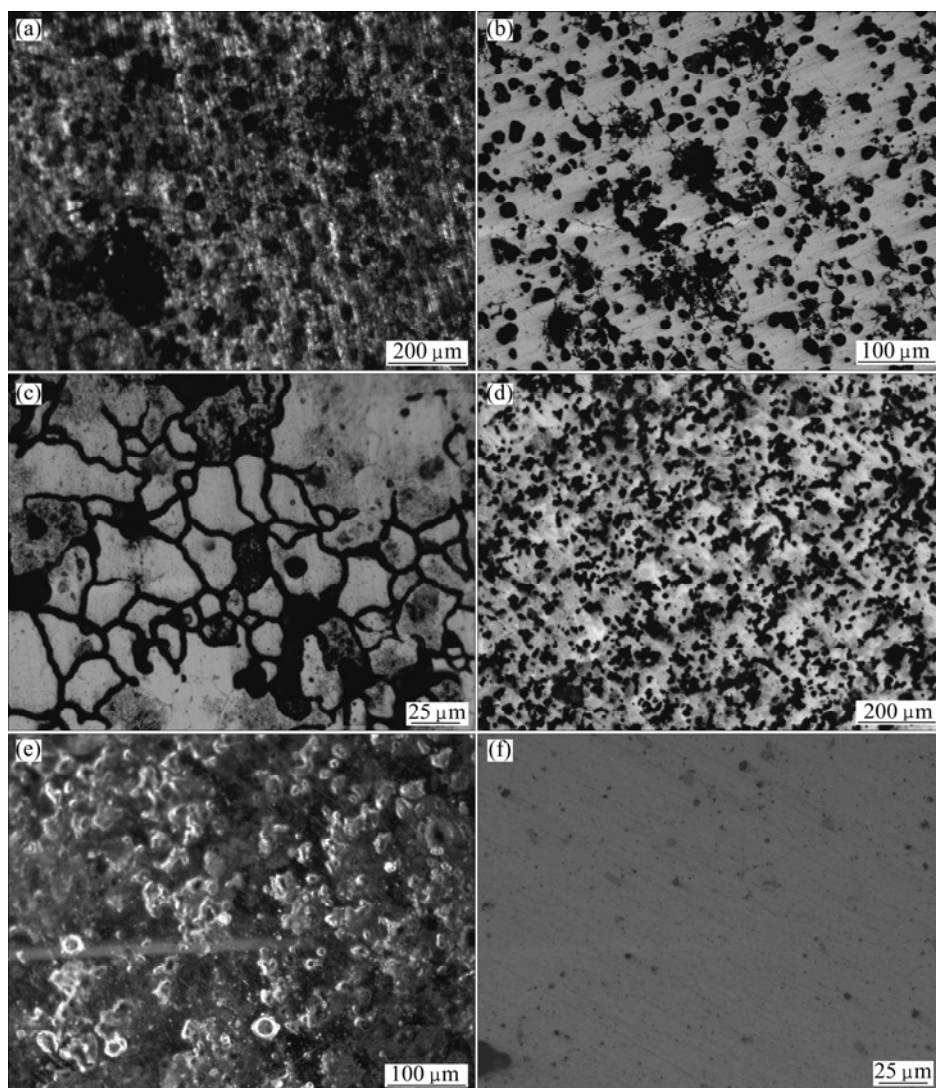
Fig. 7 Corroded surfaces of 2024 alloy: (a) Over-aged state, polarized upto −200 mV (vs SCE) in 3.5% NaCl solution; (b) As-quenched state, polarized upto 0 mV (vs SCE) in 3.5% NaCl+1.0% H₂O₂ solution; (c) Under-aged state, polarized upto −300 mV (vs SCE) in 3.5% NaCl+1.0% H₂O₂ solution; (d) Near peak-aged state, polarized upto −300 mV (vs SCE) in 3.5% NaCl solution at pH 12; (e) Dark field image of over-aged state in 3.5% NaCl solution at pH 12; (f) Near peak aged state, polarized upto −940 mV (vs SCE) in 3.5% NaCl solution at pH 12

potentiodynamic polarization run was performed on a few alloy tempers up to about 100 mV (vs SCE) below the φ_{prot} (noted from Fig. 6 at a window of decreasing current) in 3.5% NaCl solution at pH 12 and the polarizations curves are shown in Fig. 8.

The optical micrograph (Fig. 7(f)) of corroded surface of sample polarized below φ_{prot} shows that there are only a few small size scattered pits, no such extensive pitting damage, but the alloy surface is covered with a thin oxide layer because of uniform corrosion, as the alloy is polarized to about 300 mV (vs SCE) overvoltage at pH 12 that results in the dissolution of Al in alkaline condition, as discussed in section 3.4.1. The aluminium metal dissolution is also reflected in the cathodic branches of Fig. 4(c) with a higher current density compared to that in Fig. 4(a).
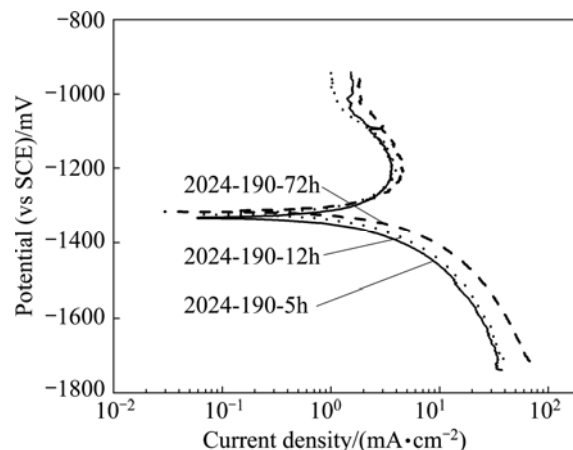

Fig. 8 Cyclic potentiodynamic polarization curves of 2024 alloy tempers run below pit protection potential in 3.5% NaCl solution at pH 12

Pitting potential may be confounded by the density of precipitate phase like *S* phase that serves as pit initiation site, possible detection of Cu depletion zones, oxide film thickness and oxide defects as well. But, φ_{rp} is associated with repassivation of large pits over a hundred times larger than any likely Cu-depleted zones, and it is believed that they reflect the corrosion properties of the matrix. Thus, the present observation of a few very small scattered pits when sample was polarized about 100 mV (vs SCE) below φ_{rp} is likely from Cu-depleted zone.

4 Conclusions

Natural and artificial ageing studies of solution heat treated and water quenched 2024 Al−Cu−Mg alloy exhibited the characteristic precipitation hardening behavior. In the peak aged state, alloy microstructure consisted of α solid solution, S' (Al$_2$CuMg) and other intermetallics phases studied by XRD and SEM. X-ray elemental mapping of a peak aged temper showed the uniform distribution of Al, Cu and Mg elements and higher proportion of Fe and Mn in the intermetallics phase areas.

Electrochemical polarization studies in 3.5% NaCl solution with or without addition of a small amount of H$_2$O$_2$ of different 2024 alloy tempers showed shifting of corrosion potential (φ_{corr}) towards more negative direction with the increase of ageing time. φ_{corr} values have been found to be less negative for the as-quenched states and more negative for the over-aged temper of the alloy, due to the reduction of copper content in the matrix α(Al) solid solution upon ageing and precipitation of *S* phase as well.

The addition of H$_2$O$_2$ in 3.5% NaCl solution resulted in shifting the corrosion potential to slightly more positive direction due to the increase of thickness of the oxide layer because of the increase of cathodic reaction (owing to more oxygen availability) that equals to higher anodic current density (i.e. dissolution of aluminium).

Polarization in 3.5% NaCl solution at pH 12 exhibited distinct passivity phenomenon. Further, φ_{corr} value of the alloy is more negative compared to that in 3.5% NaCl solution at near neutral pH. In the alkaline solution the anodic current density is dominating, and the summary current density is positive, resulting in shifting the corrosion potential to more negative values.

Cyclic potentiodynamic polarization curves showed wide open hysteresis loop, indicating that the alloy tempers are susceptible to pit growth damage. Optical micrographs of the corroded surfaces of polarized samples revealed general corrosion, extensive pitting (individual and cluster of pits), and intergranular corrosion as well, but only a few pits with less damage for the alloy when was polarized below the repassivation potential (φ_{rp}).

References

[1] ESKIN D G. Decomposition of supersaturated solid solutions in Al–Cu–Mg–Si alloys [J]. J Materials Science, 2003, 38(2): 279−290.

[2] POLMEAR I J. Light alloys metallurgy of the light metals [M]. London, UK: Arnold Publication, 1995: 24, 67.

[3] BROOKS C R. Heat treatment, structure and properties of nonferrous alloys [M]. Metals Park, Ohio, USA: American Society for Metals, 1982: 121.

[4] CHAKRABARTI D J, LAUGHIN D E. Phase relations and precipitation in Al–Mg–Si alloys with Cu additions [J]. Progress in Material Science, 2004, 49(3−4): 389−410.

[5] BUCHHEIT R G, GRANT R P, HILAVA P F, McKENZIE B, ZENDER G L. Local dissolution phenomenon associated with *S* phase (Al$_2$MgCu) particles in aluminium alloy AA 2024-T3 [J]. Electrochemical Society, 1997, 144(8): 2621−2628.

[6] BOAG A, HUGES A E, GLENN A M, MUSTER T H, McCuLLOCH D. Corrosion of 2024-T3. Part I: Localised corrosion of isolated IM particles [J]. Corrosion Science, 2011, 53(1): 17−26.

[7] DAVIS J R. Corrosion of aluminium and aluminium alloys [M]. Ohio, USA: ASM International, 1999. 1.

[8] BOAG A, HUGES A E, WILSON N C, TORPY A, MACRAE C M, GLENN A M, MUSTER T H. How complex is the microstructure of 2024-T3 [J]. Corrosion Science, 2009, 51(8): 1565−1568.

[9] ZHANG W, FRANKEL G S. Transitions between pitting and intergranular corrosion in AA 2024 [J]. Electrochemica Acta, 2003, 48(9): 1193−1210.

[10] GUILLAUMIN V, MANKOWSKI G. Localised corrosion of 2024 T351 aluminium alloy in chloride media [J]. Corrosion Science, 1999, 41(3): 421−438.

[11] WARNER T J, SCHMIDT M P, SOMMER F, BELLOT D. Characterization of corrosion initiation on 2024 aluminium alloy by atomic force microscopy [J]. Z Metallkd, 1995, 86: 494−501.

[12] CAVNAUGH M K, BIRBILIS N, BUCHHEIT R G, BOVARD F. Investigating localized corrosion susceptibility arising from Sc containing intermetallic Al$_3$Sc in high strength Al-alloys [J]. Scripta Materials, 2007, 56(11): 995−998.

[13] JONES R H, RICKER R E. Stress-corrosion cracking: Materials and evaluation [M]. Ohio, USA: ASM International, 1992: 72.

[14] GHOSH K S, DAS K, CHATTERJEE U K. Correlation of stress corrosion cracking behaviour and open circuit potential in Al−Li−Cu−Mg−Zr alloys [J]. Materials and Corrosion, 2007, 58(3): 181−187.

[15] BLANC C, LAVALLE B, MANKOWSKI G. The role of precipitates enriched with copper on the susceptibility to pitting corrosion of the 2024 aluminium alloy [J]. Corrosion Science, 1997, 39(3): 495−510.

[16] SUTER T, ALKIRE R C. Microelectrochemical studies of pit initiation at single inclusions in Al 2024-T3 [J]. Journal of Electrochemical Society, 2010, 148(1): B36−B42.

[17] BOAG A, TAYLOR R J, MUSTER T H, GOODMAN N, McCULLOCH D, RYAN C, ROUT B, JAMIESON D, HUGES A E. Stable pit formation on AA2024-T3 in an NaCl environmnent [J]. Corrosion Science, 2010, 52(1): 90−103.

[18] HUGES A E, BOAG A, GLENN A M, McCULLOCH D, MUSTER T H, RYAN C, LUO C, ZHOU X, THOMSON G E. Corrosion of 2024-T3. Part II: Co-operative corrosion [J]. Corrosion Science, 2011, 53(1): 27−39.

[19] BIRBILIS N, BUCHHEIT R G. Investigation and discussion of characteristics for intermetallic phases common to aluminum alloys as a function of solution pH [J]. Journal of Electrochemical Society, 2008, 155(3): C117−C126.

[20] BIRBILIS N, BUCHHEIT R G. Electrochemical characteristics of intermetallic phases in aluminum alloys: An experimental survey and discussion [J]. Journal of Electrochemical Society, 2005, 152(4): B140−B151.

[21] DeROSE J A, SUTER T, BALKOWIEC A, MICHALSKI J, KURZYDLOWSKI K J, SCHMUTZ P. Localised corrosion initiation and microstructural characterization of an Al 2024 alloy with a higher Cu to Mg ratio [J]. Corrosion Science, 2012, 55(2): 313−325.

[22] RALSTON K D, BIRBILIS N, CAVANAUGH M K, WEYLAND M, MUDDLE B C, MARCEAU R K W. Role of nanostructure in pitting of Al−Cu−Mg alloys [J]. Electrochemica Acta, 2010, 55(27): 7834−7842.

[23] BIRBILIS N, CAVANAUGH M K, KOVARIK L, BUCHHEIT R G. Nano-scale dissolution phenomenon in Al−Cu−Mg alloys [J]. Electrochemistry Communication, 2008, 10(1): 32−37.

[24] XIA L, AKIYAM E, FRANKEL G, McCREERY R. Storage and release of soluble hexavalent chromium from chromate conversion coatings [J]. Journal of Electrochemical Society, 2000, 147(7): 2556−2562.

[25] ZHAO J, FRANKEL G, McCREERY R L. Corrosion protection of untreated AA-2024-T3 in chloride solution by a chromate conversion coating monitored with Raman spectroscopy [J]. Journal of Electrochemical Society, 1998, 145(7): 2258−2264.

[26] LEGGAT R B, TAYLOR S R, ZHANG W, BUCHHEIT R J. Corrosion performance of field-applied chromate conversion coatings [J]. Corrosion, 2002, 58(3): 283−291.

[27] LAMAKA S V, ZHELUDKEVICH M L, YASAKAU K A, MONTEMOR M F, FERREIRA M G S. High effective organic corrosion inhibitors for 2024 aluminium alloy [J]. Electrochemica Acta, 2007, 52(25): 7231−7247.

[28] ROSERO-NAVARRO N C, CURIONI M, BINGHAM R, DURAIN A, APARICIO M, COTTIS R A, THOMSON G E. Electrochemical techniques for practical evaluation of corrosion inhibitor effectiveness. Performance of cerium nitrate as corrosion inhibitor for 2024T3 alloy [J]. Corrosion Science, 2010, 52(10): 3356−3366.

[29] MISHRA A K, BALASUBRAMANIUM R. Corrosion inhibition of aluminium alloy AA 2014 by rare earth chlorides [J]. Corrosion Science, 2007, 49(3): 1027−1044.

[30] HINTON B R W. Corrosion inhibition with rare earth metal salts [J]. Journal of Alloys and Compound, 1992, 180(1−2): 15−25.

[31] ALDYKIEWIEZ A J Jr, DAVENPORT A J, ISAACS H S. Studies of formation of cerium rich protective films using X-ray adsorption near-edge spectroscopy and rotating disk electrode methods [J]. Journal of Electrochemical Society, 1996, 143(1): 147−154.

[32] ARENAS M A, DAMBORNEA J J. Growth mechanisms of cerium layers on galvanised steel [J]. Electrochemica Acta, 2003, 48(24): 3693−3698.

[33] RAPS D, HACK, T, WEHR J, ZHELUDKEVICH M L, BASTOS A C, FERREIRA M G S, NUYKEN O. Electrochemical study of

inhibitor-containing organic–inorganic hybrid coatings on 2024 [J]. Corrosion Science, 2009, 51(5): 1012−1021.

[34] ZHELUDKEVICH M L, POZNYAK S K, RODRIGUES L M, RAPS D, HACK T, DICK L F, NUNES T, FERREIRA M G S. Active protection coatings with layered double hydroxide nanocontainers of corrosion inhibitor [J]. Corrosion Science, 2010, 52(2): 602−611.

[35] WANG S C, STARINK M J. Precipitates and intermetallic phases in precipitation hardening Al−Cu−Mg−(Li) based alloys [J]. International Materials Review, 2005, 50(4): 193−215.

[36] RINGER S P, HONO K, SAKURAI T, POLMESR I J. Cluster hardening in an aged Al−Cu−Mg alloy [J]. Scripta Materialia, 1997, 36(5): 517−521.

[37] STARINK M J, WANG S C. The thermodynamics of and strengthening due to co-clusters: General theory and application to the case of Al−Cu−Mg alloys [J]. Acta Materialia, 2009, 57(8): 2376−2389.

[38] BAGARYATSKY Y A. Dokl Akad. 1952, 87: 397−401, 559−562.

[39] CHIRAI A, WALTHER T, ALFONSO C, ZAHRA A M, ZAHRA C Y. Coexistence of clusters, GPB zones, S'', S' and S-phases in an Al−0.9%Cu−1.4%Mg alloy [J]. Acta Materialia, 2000, 48(10): 2751−2764.

[40] SHA G, MARCEAU R K W, GAO X, MUDDLE B C, RINGER S P. Nanostructure of aluminium alloy 2024: Segregation, clustering and precipitation processes [J]. Acta Materialia, 2011, 59(4): 1659−1670.

[41] RALSON K D, BIRBILIS N, WEYLAND, HUTCHINSON C R. The effect of precipitate size on yield strength-pitting corrosion correlation in Al−Cu−Mg alloys [J]. Acta Materialia, 2010, 58: 5941−5948.

[42] WANG S C, STARINK M J. Two types of S precipitates in Al−Cu−Mg alloys [J]. Acta Materialia, 2007, 55(3): 933−941.

[43] KOVARIK L, COURT S A, FRASER H L, MILLS M J. GPB zones and composite GPB/GPBII zones in Al–Cu–Mg alloys [J]. Acta Materialia, 2008, 56(17): 4804−4815.

[44] HINTON B. 2009 frank newman speller award lecture: Prevention and control of corrosion in aircraft components—Changes over four decades [J]. Corrosion, 2010, 66(8): 085001-1−15.

[45] WANG S C, STARINK M J. The assessment of GPB2/S″ structures in Al−Cu−Mg alloys [J]. Materials Science and Engineering A, 2004, 386(1−2): 156−163.

[46] HOLLINGSWORTH E H, HUNSICKER H Y. ASM Handbook [M]. Vol. 13. Materials Park, Ohio, USA: ASM International, 1992: 583.

[47] DAVIS J R. ASM specialty handbook, aluminum and aluminum alloys [M]. Ohio, USA: ASM International, The Materials Information Society, 1998: 121.

[48] GHOSH K S, MUKHOPADHYAY S, KONAR B, MISRA B. Study of aging and electrochemical behaviour of Al−Li−Cu−Mg alloys [J]. Materials and Corrosion, 2012, 63. DOI:10.1002/maco.201106409.

[49] ANTROPOV L I. Theoretical electrochemistry [M]. Moscow: Mir Publication, 1972: 503.

[50] SCULLY J R, KNIGHT T O, BUCHHEIT R G, PEEBLES D E. Electrochemical characteristics of the Al_2Cu, Al_3Ta and Al_3Zr intermetallic phases and their relevancy to the localized corrosion of Al alloys [J]. Corrosion Science, 1993, 35(1−4): 185−195.

[51] McCAFFERTY E. The electrode kinetics of pit initiation on aluminum [J]. Corrosion Science, 1995, 37(3): 481−492.

[52] SCULLY J H. ASM Handbook [M]. Vol. 13A. Ohio, USA: ASM International, 2003: 68.

不同热处理态 **2024** 铝合金的腐蚀行为

K. S. GHOSH, Md. HILAL, Sagnik BOSE

Department of Metallurgical and Materials Engineering, National Institute of Technology, Durgapur – 713 209, India

摘　要： 分别在 3.5% NaCl 溶液、3.5% NaCl+1.0% H_2O_2 溶液和 pH=12 的 3.5% NaCl 溶液中进行动电位极化实验，研究 2024 Al−Cu−Mg 合金在不同热处理状态下的腐蚀行为。极化曲线表明，随着合金时效时间的延长，合金的腐蚀电位向负方向移动；向 NaCl 溶液中添加 H_2O_2 会使腐蚀电位正移；在 pH=12 的 3.5% NaCl 溶液中的极化曲线表现出明显的钝化现象。腐蚀试样表面表现为常见的腐蚀特征，但也有扩大的点蚀、晶间腐蚀现象出现。循环动电位极化曲线显示有宽的循环极化滞后环，不同的腐蚀模式表明合金的点蚀生长对合金的热处理状态敏感。通过显微组织分析，探讨了不同热处理状态下合金在不同 NaCl 溶液中的腐蚀机理。

关键词： 2024 铝合金；时效行为；电化学极化；钝化；点蚀电位

(Edited by Sai-qian YUAN)